

# Acoustic Tomography of the Atmosphere Using Unscented Kalman Filter

Soheil Kolouri, Mahmood R. Azimi-Sadjadi, *Senior Member, IEEE*, and Astrid Ziemann

**Abstract**—Acoustic travel-time tomography of the atmosphere is a nonlinear inverse problem which attempts to reconstruct temperature and wind velocity fields in the atmospheric surface layer using the dependence of sound speed on temperature and wind velocity fields along the propagation path. This paper presents a new statistical-based acoustic travel-time tomography algorithm based on unscented Kalman filter (UKF) which is capable of reconstructing and tracking temperature and wind velocity fields (state variables) within a specified investigation area. The method exploits an iterative ray-tracing algorithm to handle situations when straight-ray assumption no longer holds. The observations used in the UKF process consists of the acoustic travel times computed for every pair of transmitter/receiver nodes deployed in the investigation area. A first-order spatial-temporal autoregressive model is used to account for state evolution in the UKF. To evaluate the performance of the UKF-based acoustic tomography method, 2-D fractal Brownian motion is used to generate synthetic temperature and wind velocity fields with spatial and temporal resolution of 1 m and 12 s, respectively. The UKF-based acoustic tomography algorithm is then compared to the well-known time-dependent stochastic inversion method. The results reveal the effectiveness of the proposed method for accurate and fast reconstruction of temperature and wind velocity fields.

**Index Terms**—Acoustic tomography, fractal Brownian motion, unscented Kalman filter.

## I. INTRODUCTION

MONITORING temperature and wind velocity fields in the atmospheric surface layer has always been of great importance in different disciplines such as boundary layer meteorology [1]–[4] and studies of sound propagation through a turbulent atmosphere [5]. Spatially resolved temperature and wind velocity fields are needed as adequate input data for the evaluation of atmospheric models. Furthermore, such data can be applied to investigate the effects of an inhomogeneous surface on the energy exchange between the surface and the atmosphere. The conventional approach to measuring these

fields is to use *in situ* thermo-anemometers. However employing these sensors within the investigation area has two major drawbacks. First, this is not an economically viable solution, as a large number of such rather expensive sensors are needed to achieve an acceptable spatial resolution. Moreover, deploying these sensors in an investigation area may distort the measured fields. Therefore, remote sensing methods [6]–[9] such as acoustic tomography, sonic detection and ranging, radio acoustic sounding system, and light detection and ranging are among the alternative choices.

Acoustic tomography<sup>1</sup> [6], [10]–[14] has been successfully used to measure temperature and wind velocity fields with minimal interference in the investigation area and lesser cost. The main advantages of the acoustic tomography method are: 1) the ability to provide spatially and temporally resolved fields useful for model evaluation; 2) the ability to simultaneously reconstruct temperature and wind velocity fields with the same resolution; and 3) scalability property achieved by adapting the transmitters and receivers. Unlike the forward problems [15], which aim at estimating properties of the signal at the receivers such as the transmission loss, given the temperature and wind velocity fields, ground conditions, and the characteristics of the sound sources and their locations with respect to the sensors, acoustic tomography (inverse problem) [6], [10]–[14] aims at estimating temperature and wind velocity fields given the characteristics of the sound sources, the coordinates of sensors, and the travel time for acoustic propagation paths.

Acoustic tomography was extensively studied in underwater acoustics for many years (see [16], [17]). Later, Spiesberger, and Fristrup [18] investigated the problem of locating birds' calls based on the received signatures using acoustic tomography. They demonstrated that consideration of temperature and wind flow along the sound propagation paths can significantly improve the accuracy of localization. Wilson and Thomson [6] conducted an acoustic tomography experiment with actual sound sources and microphones to measure the atmospheric surface layer temperature and wind velocity fields. They showed that using acoustic tomography is highly beneficial, as it uses a small number of acoustic sensors to reconstruct the temperature and wind velocity fields with high spatial resolution.

Solving an acoustic tomography problem is in general difficult, owing to its generally nonlinear nature. Several

Manuscript received June 29, 2012; revised December 21, 2012 and April 9, 2013; accepted April 10, 2013. Date of publication May 27, 2013; date of current version January 2, 2014. This work was supported by the DoD Center for Geosciences/Atmospheric Research at Colorado State University under Cooperative Agreement W911NF-06-2-0015 with the Army Research Laboratory.

S. Kolouri and M. R. Azimi-Sadjadi are with the Department of Electrical and Computer Engineering, Colorado State University, Fort Collins, CO 80523-1373 USA (e-mail: kolouri@engr.colostate.edu; azimi@engr.colostate.edu).

A. Ziemann is with the Institute of Hydrology and Meteorology, Technische Universität Dresden, Dresden 01062, Germany (e-mail: astrid.ziemann@tu-dresden.de).

Color versions of one or more of the figures in this paper are available online at <http://ieeexplore.ieee.org>.

Digital Object Identifier 10.1109/TGRS.2013.2258401

<sup>1</sup>Note: throughout this paper, “acoustic tomography” is used frequently instead of “acoustic time-travel tomography.”

algorithms have been introduced in different fields to solve this inverse problem [6], [11], [13]. These algorithms are commonly categorized as statistical-based algorithms [6], [10], [13], [14], algebraic-based algorithms [11], [12], [19]–[22], and those that use a sparse reconstruction framework [23].

Wilson and Thomson [6] developed a statistical-based algorithm, referred to as stochastic inversion (SI), to reconstruct the temperature and wind velocity fields. This method is based on linear minimum variance (LMV) estimation [24], which assumes certain (e.g., Gaussian) spatial auto-correlation and cross-correlation functions for statistically homogenous (in space) turbulence. Owing to its linearity assumption,<sup>2</sup> estimates of the unknown fields will be linear combinations of the observed acoustic travel time. SI separates this estimation problem into estimating mean fields and fluctuations, assuming low to nominal wind conditions and using models for the spatial correlations to reconstruct temperature and wind velocity fields. Vecherin *et al.* [13] and [14] proposed a modified version of SI algorithm referred to as time-dependent stochastic inversion (TDSI), which uses an augmented vector of several snapshots in time as the observation vector. Similar to SI, it employs an LMV estimator to reconstruct the fluctuation fields and uses explicit correlation functions. The locally frozen turbulence assumption is also used in TDSI to formulate the spatial-temporal covariance functions that are needed to apply the LMV estimator.

Among the algebraic-based algorithms are the algebraic reconstruction techniques including multiplicative algebraic reconstruction technique [25] and simultaneous iterative reconstruction technique [11], [26]. By separating the influence of temperature and wind velocity fields, they reformulate the problem linearly. The linear system is then solved by an iterative  $\ell_2$ -norm minimization using gradient-based methods. The process starts from some initial values for the fields and calculates the travel time along known sound ray paths. Then, the deviations between the calculated travel time and the actual measured values are calculated, and adjustments are made to the initial fields until the deviations between the calculated and measured travel time values are small.

The unscented Kalman filter (UKF) and particle filters have been applied in the past to geoacoustic inversion problems [27] where certain environmental parameters such as water column and seabed properties are tracked in time and space. In this paper, a new statistical-based approach for solving the inverse acoustic problem is presented using UKF [28], [29]. The investigation area is discretized into grids in which the temperature and wind velocity fields are assumed to be spatially constant. The state vector is formed of the temperature and wind velocity fields in all grids covering the monitored area. The observation vector consists of the noisy acoustic travel time measurements for every pair of transmitter/receivers nodes. UKF is then employed for this generally nonlinear state-estimation problem to estimate and track the states at every time snapshot with initial states that are chosen

to be the temperature and wind velocity spatial mean fields. The proposed method uses a 3-D autoregressive (AR) model to capture the spatiotemporal dynamics of the temperature and wind velocity fields and offers a robust and accurate solution to this inverse acoustic problem. The effectiveness of the proposed UKF-based acoustic tomography method is demonstrated on synthesized data generated using 2-D fractal Brownian motion (fBm) [30].

The rest of this paper is organized as follows. Section II reviews the acoustic tomography inverse problem formulation and summarizes the statistical-based algorithm TDSI used frequently in acoustic tomography. The proposed inverse acoustic tomography method is described in detail in Section III. Section IV describes the synthetic data generation process and compares the results of TDSI-based acoustic tomography algorithm with those of the proposed method. Finally, Section V presents a brief conclusion on the results and the contributions of this paper.

## II. PROBLEM FORMULATION

### A. Review of Acoustic Propagation Formulation

The travel time for an acoustic wave to propagate from a source to a receiver is a function of the temperature, wind velocity (air flow), and humidity along the path [2], [6], [10]–[14]. However, compared to the influence of temperature and flow (and their local inhomogeneities), the contribution of humidity on the travel time is secondary [26]. Acoustic tomography methods use this relation to reconstruct the temperature and wind velocity in an investigation area based on several travel time measurements between different sources and receivers deployed in the area. In the absence of wind, the acoustic wavefront propagates with adiabatic sound speed [6] given by

$$c_L^2 = \gamma_a R_a T_{av} \quad (1)$$

where  $\gamma_a \approx 1.41$  denotes the ratio of specific heat capacities at constant pressure and volume for dry air;  $R_a$  is the specific gas constant for dry air (287.05 J/K·kg); and  $T_{av}$  is the acoustic virtual temperature, which is related to the thermodynamic temperature  $T_{th}$  as  $T_{av} = T_{th}(1 + 0.511q)$ , with  $q$  being the specific humidity defined as the mass ratio of water vapor to moist air [4].

In the field experiments, though, wind velocity significantly impacts the speed of sound propagating along a specific path. The wind velocity can be formulated as

$$\mathbf{v}(\mathbf{r}, t) = \alpha(\mathbf{r}, t) \cos(\theta(\mathbf{r}, t))\mathbf{e}_x + \alpha(\mathbf{r}, t) \sin(\theta(\mathbf{r}, t))\mathbf{e}_y \quad (2)$$

where  $\mathbf{e}_x$  and  $\mathbf{e}_y$  are the unit vectors of a 2-D Cartesian coordinate system,  $\mathbf{r} = x\mathbf{e}_x + y\mathbf{e}_y$  is the position vector of a point on the investigation area, and  $\alpha(\mathbf{r}, t)$  and  $\theta(\mathbf{r}, t)$  are the magnitude and direction of the wind velocity at position  $\mathbf{r}$  and time  $t$ , respectively. Therefore, the sound speed along the sound ray can be defined as

$$c_{ray}(\mathbf{r}, t) = \mathbf{s} \cdot (c_L(\mathbf{r}, t) \cdot \mathbf{n} + \mathbf{v}(\mathbf{r}, t)) \quad (3)$$

where  $\mathbf{s}$  and  $\mathbf{n}$  denote the unit vectors in the direction of sound propagation and normal to the wavefront, respectively. From

<sup>2</sup>The validity of this assumption depends on the magnitude of wind velocity wrt sound speed; i.e., as wind speed increases, the assumption of linearity becomes less acceptable.

(3), it can be shown [6] that for a source and receiver with 100 m separation, a path-averaged fluctuation as small as  $1\frac{m}{s}$  in the wind velocity produces approximately 0.9 ms fluctuation in the travel time, whereas a path-averaged fluctuation as small as  $1^\circ\text{C}$  in the temperature causes approximately 0.6 ms fluctuation in the travel time.

The simplest ray model for acoustic propagation is the straight-ray model which is typically used in most literature. The straight-ray model is valid for sound propagation distances of few hundreds of meters, when the temperature and wind velocity fields are smooth and the speed of wind is less than the adiabatic sound speed  $c_L$ . The straight-ray model implies that  $\mathbf{s}$  and  $\mathbf{n}$  are in the same direction, hence  $\mathbf{s} \cdot \mathbf{n} \approx 1$ . However, in presence of large temperature or wind velocity gradients or high wind speed, using the straight-ray model leads to nonunique solutions of the wind velocity field. In [23], the authors suggested using the time-difference of arrivals among tripoles of transmitters and receivers to estimate the angles of departure/arrival (hence  $\mathbf{n}_T$  and  $\mathbf{n}_R$  at these pairs of sensor triploes) of the sound wave. A linear fit (e.g., using the least-squares method) can then be employed to produce the estimate of  $\mathbf{n}(\mathbf{r}, t)$  between these points given the path. Ray tracing can also be employed in this bent-ray model to estimate  $\mathbf{s}(\mathbf{r}, t)$  along the path based on prior estimates of the temperature and wind fields

$$\mathbf{s}(\mathbf{r}, t) = \frac{\mathbf{n}c_L(\mathbf{r}, t-1) + \mathbf{v}(\mathbf{r}, t-1)}{\|\mathbf{n}c_L(\mathbf{r}, t-1) + \mathbf{v}(\mathbf{r}, t-1)\|} \quad (4)$$

where initially one can start with straight rays as the first approximations. As new wind and temperature field reconstructions become available, the accuracy of ray tracing improves. Note that here 2-D (i.e., horizontal projection) ray propagation and refraction is considered, though this is a truly 3-D phenomenon when including vertical temperature and wind gradients. In Section III, we shall see how this bent-ray model can be incorporated into the proposed UKF-based reconstruction method.

Once  $\mathbf{s}(\mathbf{r}, t)$  and  $\mathbf{n}(\mathbf{r}, t)$  are estimated along each path, (3) can be rewritten as

$$c_{\text{ray}}(\mathbf{r}, t) = \zeta(\mathbf{r}, t)c_L(\mathbf{r}, t) + \mathbf{s}(\mathbf{r}, t) \cdot \mathbf{v}(\mathbf{r}, t) \quad (5)$$

where  $\zeta(\mathbf{r}, t) = \mathbf{s}(\mathbf{r}, t) \cdot \mathbf{n}(\mathbf{r}, t)$ .

Based on (5), which is a well-known relation for the effective sound speed [4], the travel time formula for the  $n$ th path is defined as

$$\tau_n(t) = \int_{L_n} \frac{dl_n}{c_{\text{ray}}(\mathbf{r}, t)} = \int_{L_n} \frac{dl_n}{\zeta_n(\mathbf{r}, t)c_L(\mathbf{r}, t) + \mathbf{s}_n(\mathbf{r}, t) \cdot \mathbf{v}(\mathbf{r}, t)} \quad (6)$$

where the integration is along the  $n$ th propagation path,  $L_n$  is the length of the  $n$ th propagation path, and  $\mathbf{s}_n(\mathbf{r}, t)$  is the unit vector in the direction of the wave propagation at location  $\mathbf{r}$  and time snapshot  $t$ .

In order to be able to estimate the fields in the investigation area, almost all existing methods [6], [10]–[14], [20], [26] discretize the investigation area into several points of interest. Here, we use  $I \times J$  grids in which we assume that  $c_L(\mathbf{r}, t)$

and  $\mathbf{v}(\mathbf{r}, t)$  are spatially constant. Thus, (6) can be discretized as

$$\tau_n(t) = \sum_{i=1}^I \sum_{j=1}^J \frac{d_n(i, j)}{\zeta_n([i, j], t)c_L([i, j], t) + \mathbf{s}_n([i, j], t) \cdot \mathbf{v}([i, j], t)} \quad (7)$$

Here,  $d_n(i, j)$  is the distance that the  $n$ th propagation path travels in the  $(i, j)$ th cell, and  $c_L([i, j], t)$  and  $\mathbf{v}([i, j], t)$  are the adiabatic sound speed and the wind velocity vector in the  $(i, j)$ th grid at time  $t$ , respectively.

The term  $\mathbf{s}_n([i, j], t) \cdot \mathbf{v}([i, j], t)$  in (7) can be written as

$$\begin{aligned} \mathbf{s}_n \cdot \mathbf{v}([i, j], t) &= \alpha([i, j], t) \cos(\theta([i, j], t)) \cos(\phi_n[i, j], t)) \\ &\quad + \alpha([i, j], t) \sin(\theta([i, j], t)) \sin(\phi_n[i, j], t)) \end{aligned} \quad (8)$$

where  $\alpha([i, j], t)$  and  $\theta([i, j], t)$  are, respectively, the amplitude and angle (with respect to  $\mathbf{e}_x$ ) of the wind velocity in the  $(i, j)$ th grid at time  $t$ , and  $\phi_n[i, j], t)$  is the angle of  $\mathbf{s}_n[i, j], t)$  with  $\mathbf{e}_x$ .

The goal of acoustic tomography is then to find  $c_L([i, j], t)$ ,  $\alpha([i, j], t)$  and  $\theta([i, j], t)$ , for  $i = 1, \dots, I$  and  $j = 1, \dots, J$ , given coordinates of the acoustic transmitter and receiver tripole sets deployed in the field and the travel times between each transmitter and receiver, i.e.,  $\tau_n(t)$ s, recorded for all propagation paths and at each snapshot  $t$ .

### B. A Review of TDSI Method

As mentioned before, TDSI [13], [14] is based on linearizing (6) and decomposing temperature and wind velocity fields into spatial mean fields and spatial fluctuation fields using the straight-ray assumption, i.e.,  $\mathbf{s} \cdot \mathbf{n} \approx 1$ . For instance, for the adiabatic sound speed we have  $c_L([i, j], t) = \bar{c}_L(t) + \tilde{c}_L([i, j], t)$ , where  $\bar{c}_L(t)$  and  $\tilde{c}_L([i, j], t)$  are the mean and fluctuation components, respectively. Similar equations exist for  $T_{\text{av}}([i, j], t)$ ,  $\alpha([i, j], t)$ , and  $\theta([i, j], t)$  [6], [13]. Since the fluctuations are small compared to the mean fields, (6) can be approximated by its first-order expansion [13] as

$$\begin{aligned} \tau_n(t) &= \frac{L_n}{\bar{c}_L^2(t)} (\bar{c}_L - \bar{\alpha}(t) \cos(\bar{\theta}(t))) \cos(\phi_n) \\ &\quad - \bar{\alpha}(t) \sin(\bar{\theta}(t)) \sin(\phi_n) \\ &\quad - \frac{1}{\bar{c}_L^2(t)} \int_{L_n} dl_n \left( \frac{\tilde{c}_L(t)}{2T_{\text{av}}(t)} \tilde{T}_{\text{av}}(\mathbf{r}, t) \right. \\ &\quad \left. + \tilde{\alpha}(\mathbf{r}, t) \cos(\tilde{\theta}(r, t)) \cos(\phi_n) \right. \\ &\quad \left. + \tilde{\alpha}(\mathbf{r}, t) \sin(\tilde{\theta}(r, t)) \sin(\phi_n) \right) + \epsilon_n(t) \end{aligned} \quad (9)$$

where  $\epsilon_n(t)$  represents the effects of the linearization and measurement errors for the  $n$ th path at time  $t$ .

In order to estimate the mean fields, fluctuations in (9) are first neglected, in which case the integral vanishes and the remaining part forms an overdetermined system of  $N$  (number of paths) linear equations with three unknowns, which can easily be solved by the LS method [24].

By employing the mean fields and (9), a new observation  $q_n(t)$  for the  $n$ th path at snapshot  $t$  is

$$\begin{aligned} q_n(t) &\triangleq L_n (\bar{c}_L(t) - \bar{\alpha}(t) \cos(\bar{\theta}(t)) \cos(\phi_n) \\ &\quad - \bar{\alpha}(t) \sin(\bar{\theta}(t)) \sin(\phi_n)) - \bar{c}_L^2(t) \tau_n(t). \end{aligned} \quad (10)$$

$$q_n(t) = \sum_{i=1}^I \sum_{j=1}^J d_n(i, j) \left( \frac{\bar{c}(t)}{2\bar{T}_{av}(t)} \tilde{T}_{av}([i, j], t) + \tilde{\alpha}([i, j], t) \cos(\tilde{\theta}([i, j], t)) \cos(\phi_n) \right. \\ \left. + \tilde{\alpha}([i, j], t) \sin(\tilde{\theta}([i, j], t)) \sin(\phi_n) \right) + \bar{c}_L^2(t) \epsilon_n(t) \quad (12)$$

Using this new observation, (9) is reformulated as

$$q_n(t) = \int_{L_n} dl_n \left( \frac{\bar{c}(t)}{2\bar{T}_{av}(t)} \tilde{T}_{av}(\mathbf{r}, t) \right. \\ \left. + \tilde{\alpha}(\mathbf{r}, t) \cos(\tilde{\theta}(\mathbf{r}, t)) \cos(\phi_n) \right. \\ \left. + \tilde{\alpha}(\mathbf{r}, t) \sin(\tilde{\theta}(\mathbf{r}, t)) \sin(\phi_n) \right) + \bar{c}_L^2(t) \epsilon_n(t). \quad (11)$$

Now, discretizing (11) into  $I \times J$  points yields (12), shown at the top of the page.

If we arrange all  $N$  observations for all paths at time  $t$  into a column vector  $\mathbf{q}(t) = [q_1(t), \dots, q_N(t)]$  and all fluctuations to be reconstructed into a column vector  $\mathbf{m}(t) = [\tilde{T}_{av}([1, 1], t), \dots, \tilde{T}_{av}([I, J], t), \tilde{\alpha}([1, 1], t), \dots, \tilde{\alpha}([I, J], t), \tilde{\theta}([1, 1], t), \dots, \tilde{\theta}([I, J], t)]^T$ , then the problem is cast as a linear system.

TDSI uses the past  $M$  snapshots and forms the augmented observation vector  $\mathbf{q}_a(t) = [\mathbf{q}(t-M), \mathbf{q}(t-M+1), \dots, \mathbf{q}(t)]^T$  to reconstruct vector  $\mathbf{m}(t)$ , using LMV estimator

$$\hat{\mathbf{m}}(t) = C_{mq_a} C_{q_a q_a}^{-1} \mathbf{q}_a(t) \quad (13)$$

where  $C_{mq_a} = \langle \mathbf{m} \mathbf{q}_a^T \rangle$  is the model data cross-covariance matrix and  $C_{q_a q_a} = \langle \mathbf{q}_a \mathbf{q}_a^T \rangle$  is the data auto-covariance matrix [13, eqs. (18)–(21)], and  $\langle \cdot \rangle$  represents the time averaging. Assuming that the adiabatic sound speed and wind velocity fields are stationary,  $C_{mq_a}$  and  $C_{q_a q_a}$  are defined as follows:

$$C_{mq_a} = [B_{mq}(-M), B_{mq}(-M+1), \dots, B_{mq}(0)] \quad (14)$$

$$C_{q_a q_a} = \begin{bmatrix} B_{qq}(0) & B_{qq}(1) & \dots & B_{qq}(M) \\ B_{qq}(-1) & B_{qq}(0) & \dots & B_{qq}(M-1) \\ \vdots & \vdots & \ddots & \vdots \\ B_{qq}(-M) & B_{qq}(-M+1) & \dots & B_{qq}(0) \end{bmatrix} \quad (15)$$

where  $B_{mq}(\Delta t = t_k - t_l) = \langle \mathbf{m}(t_l) \mathbf{q}^T(t_k) \rangle$  is the cross-covariance matrix of size  $3IJ \times N$  between  $\mathbf{m}$  at time  $t_l$  and the observation vector  $\mathbf{q}$  at time  $t_k$ , and  $B_{qq}(\Delta t = t_k - t_l) = \langle \mathbf{q}(t_l) \mathbf{q}^T(t_k) \rangle$  is the covariance matrix of size  $N \times N$  between the observations at times  $t_l$  and  $t_k$ . These matrices are defined explicitly based on the spatiotemporal correlation functions. The reader is referred to [13] for a detailed description of these matrices.

### III. INVERSE ACOUSTIC TOMOGRAPHY USING UKF METHOD

UKF is an extension of classical Kalman filter [31] for nonlinear state estimation problems. Unlike the extended Kalman filter [32] which uses the first-order approximation of the nonlinear system, UKF represents a derivative-free alternative with lesser computational complexity. UKF employs the unscented transform [29], [33] to estimate the distribution of an *a posteriori* state without the need for any linearization.

Unscented transform estimates the distribution of a random variable by computing the sigma points and propagating them through the nonlinear functions. To use the UKF, state and observation equations must be formed.

The adiabatic sound speed, wind velocity amplitude, and wind velocity angle at all grids are arranged to form the state vector

$$\mathbf{x}_t = [\mathbf{c}_L^T(t), \boldsymbol{\alpha}^T(t), \boldsymbol{\theta}^T(t)]^T \quad (16)$$

where  $\mathbf{c}_L(t) = [c_L([1, 1], t), c_L([1, 2], t), \dots, c_L([I, J], t)]^T$  is the column vector of the adiabatic sound speeds at every grid, and similarly for  $\boldsymbol{\alpha}(t)$  and  $\boldsymbol{\theta}(t)$ . Note that  $\mathbf{x}_t$  is a column vector of length  $L = 3I * J$ . The observation vector  $\mathbf{y}_t$ , on the other hand, consists of travel time measurements for all acoustic propagation paths

$$\mathbf{y}_t = [\tau_1(t), \dots, \tau_N(t)]^T \quad (17)$$

where  $\tau_i(t)$  is the travel time for the  $i$ th path at snapshot  $t$ .

#### A. State Evolution Process

To capture the spatiotemporal state dynamics for adiabatic sound speed and wind velocity amplitude, we use a 3-D AR model that relates these fields at grid  $[i, j]$  and snapshot  $t$  to those at the adjacent grids at time  $t - 1$ . This forms the spatiotemporal support region for each grid at time  $t$ . For wind velocity angle, however, a random walk model is used because of the erratic behavior of this component. The state evolution equation for the adiabatic sound speed at a specific grid  $[i, j]$  is defined as

$$c_L([i, j], t) = \rho_0^{c_L} c_L([i, j], t-1) + \rho_1^{c_L} (c_L([i+1, j], t-1) \\ + c_L([i, j+1], t-1) + c_L([i-1, j], t-1) \\ + c_L([i, j-1], t-1)) + \rho_2^{c_L} (c_L([i-1, j-1], \\ \times t-1) + c_L([i-1, j+1], t-1) \\ + c_L([i+1, j-1], t-1) \\ + c_L([i+1, j+1], t-1)) + u_{c_L}([i, j], t) \quad (18)$$

where  $\rho_0^{c_L}$ ,  $\rho_1^{c_L}$ , and  $\rho_2^{c_L}$  are the AR model coefficients, and  $u_{c_L}([i, j], t)$  is the driving noise which represents the inaccuracies in the modeling of the state evolution in time. Fig. 1 shows the spatiotemporal support region of this 3-D AR model for the adiabatic sound speed field at time  $t$ . Note that, around the boundaries, the support region of a cell is confined to its neighbors within the investigation area.

This AR model for the adiabatic sound speed field can be expressed in the vector form as

$$\mathbf{c}_L(t) = \mathbf{A}^{(c_L)} \mathbf{c}_L(t-1) + \mathbf{u}_{c_L}(t) \quad (19)$$

where  $\mathbf{u}_{c_L}(t) = [u_{c_L}([1, 1], t), \dots, u_{c_L}([I, J], t)]^T$  is the column vector of the adiabatic sound speed driving process.

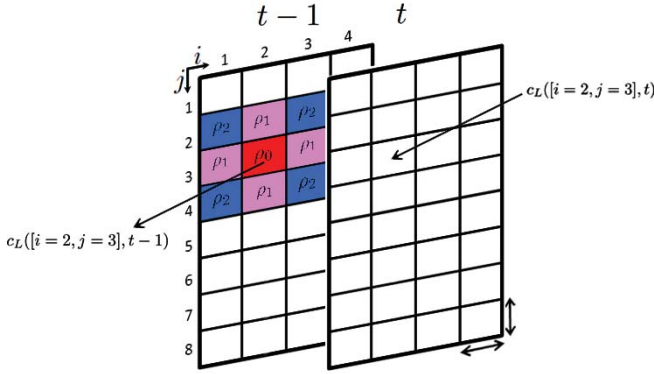


Fig. 1. Spatiotemporal support region of 3-D AR model.

Matrix  $A^{(cL)}$  is a block Toeplitz matrix, with the Toeplitz blocks given by

$$A^{(cL)} \triangleq \begin{bmatrix} B & C & \mathbf{0} & \mathbf{0} & \mathbf{0} & \mathbf{0} & \mathbf{0} & \mathbf{0} \\ C & B & C & \mathbf{0} & \mathbf{0} & \mathbf{0} & \mathbf{0} & \mathbf{0} \\ \mathbf{0} & C & B & C & \mathbf{0} & \mathbf{0} & \mathbf{0} & \mathbf{0} \\ \mathbf{0} & \mathbf{0} & C & B & C & \mathbf{0} & \mathbf{0} & \mathbf{0} \\ \mathbf{0} & \mathbf{0} & \mathbf{0} & C & B & C & \mathbf{0} & \mathbf{0} \\ \mathbf{0} & \mathbf{0} & \mathbf{0} & \mathbf{0} & C & B & C & \mathbf{0} \\ \mathbf{0} & \mathbf{0} & \mathbf{0} & \mathbf{0} & \mathbf{0} & C & B & C \\ \mathbf{0} & \mathbf{0} & \mathbf{0} & \mathbf{0} & \mathbf{0} & \mathbf{0} & C & B \end{bmatrix} \quad (20)$$

and the B and C block matrices are defined as

$$B = \begin{bmatrix} \rho_0^{cL} & \rho_1^{cL} & 0 & 0 \\ \rho_1^{cL} & \rho_0^{cL} & \rho_1^{cL} & 0 \\ 0 & \rho_1^{cL} & \rho_0^{cL} & \rho_1^{cL} \\ 0 & 0 & \rho_1^{cL} & \rho_0^{cL} \end{bmatrix} \quad (21)$$

$$C = \begin{bmatrix} \rho_1^{cL} & \rho_2^{cL} & 0 & 0 \\ \rho_2^{cL} & \rho_1^{cL} & \rho_2^{cL} & 0 \\ 0 & \rho_2^{cL} & \rho_1^{cL} & \rho_2^{cL} \\ 0 & 0 & \rho_2^{cL} & \rho_1^{cL} \end{bmatrix}. \quad (22)$$

The AR coefficients  $\rho_0^{cL}$ ,  $\rho_1^{cL}$ , and  $\rho_2^{cL}$  are estimated based on the Yule–Walker method [34] using either a training dataset if *in situ* measurements are available or assuming a specific spatiotemporal correlation structure for each field and estimating its parameters using some training data. The latter is the approach taken here. Similar relationships holds for  $\alpha(t)$ , whereas a random walk model is used for  $\theta(t)$ . Thus, we have

$$\begin{aligned} \alpha(t) &= A^{(\alpha)}\alpha(t-1) + \mathbf{u}_\alpha(t) \\ \theta(t) &= \theta(t-1) + \mathbf{u}_\theta(t). \end{aligned} \quad (23)$$

Here,  $\mathbf{u}_\alpha(t)$  and  $\mathbf{u}_\theta(t)$  are, respectively, the driving processes for amplitude and the angle of wind velocity and matrix  $A^{(\alpha)}$  is defined in a similar manner as  $A^{(cL)}$ . Note that the AR models are assumed to be decoupled from each other, as the phenomena that generate them are independent. Note that this is the main reason behind defining the wind state variables as amplitude and angle instead of the two dependent components. Combining these decoupled equations yields the following state equation

$$\mathbf{x}_t = A\mathbf{x}_{t-1} + \mathbf{u}_t \quad (24)$$

where  $\mathbf{u}_t = [\mathbf{u}_{cL}(t)^T, \mathbf{u}_\alpha(t)^T, \mathbf{u}_\theta(t)^T]^T$  is the augmented driving noise vector which is assumed to be Gaussian with zero mean and known covariance matrix  $R_u$ , and matrix A is

$$A = \begin{bmatrix} A^{(cL)} & \mathbf{0} & \mathbf{0} \\ \mathbf{0} & A^{(\alpha)} & \mathbf{0} \\ \mathbf{0} & \mathbf{0} & \mathbf{I} \end{bmatrix}. \quad (25)$$

### B. Observation Process

The relationship between state  $\mathbf{x}_t$  and observation vector  $\mathbf{y}_t$  at time  $t$  is given by (7), (8), and (17), and is a nonlinear function of the state variables expressed as

$$\mathbf{y}_t = H(\mathbf{x}_t) + \mathbf{v}_t \quad (26)$$

where  $\mathbf{v}_t$  stands for measurement noise caused by such things as: 1) errors inherent in the gridding process; 2) error in measuring the travel times; and 3) sensor location uncertainty, and it is assumed to be a Gaussian random vector with zero mean and known covariance matrix,  $R_v$ . Among these sources the most dominant is the first one. The nonlinear function  $H(\mathbf{x}_t)$  is explicitly defined as

$$H(\mathbf{x}_t) = \begin{bmatrix} \sum_{i=1}^I \sum_{j=1}^J \frac{d_1(i,j)}{\xi_1([i,j],t)_{cL}([i,j],t) + \mathbf{s}_1([i,j],t) \cdot \mathbf{v}([i,j],t)} \\ \vdots \\ \sum_{i=1}^I \sum_{j=1}^J \frac{d_N(i,j)}{\xi_N([i,j],t)_{cL}([i,j],t) + \mathbf{s}_N([i,j],t) \cdot \mathbf{v}([i,j],t)} \end{bmatrix}. \quad (27)$$

### C. Fixed-Point Iterative UKF Equations

In the case of large uncertainty in the choice of the initial error covariance matrix and weak observability of the system, UKF exhibits slow convergence and poor state estimation accuracy. Iterated UKF [35] is a more robust version of UKF which not only iterates on every snapshot  $t$  but also performs a fixed-point iteration at each fixed snapshot to get more accurate state estimates.

To apply fixed-point iterative UKF to any nonlinear state estimation process, one needs to generate estimates of covariance matrices  $R_u$  and  $R_v$  for the driving noise and measurement noise, respectively. The covariance matrix  $R_u$  is generally estimated using either training data or assuming a spatiotemporal correlation as mentioned before. The covariance matrix  $R_v$ , on the other hand, can be estimated from typical measurement data and the error in the measurement devices. Given these matrices and defining  $\mathbf{x}_{k|k}(t)$  to be the state estimate at  $k$ th iteration of snapshot  $t$ , the fixed-point iterative UKF steps for  $k \in [0, K]$  iterations on each snapshot  $t$  are as follows.

1) *Initialization*: Fixed-point iterative UKF starts by initializing the state vector estimate  $\hat{\mathbf{x}}_{K|K}(0)$  (i.e., estimate of state vector at time  $t = 0$ ) as the mean field generated using the method explained in Section II-B. Additionally, the corresponding state error covariance matrix  $P_{K|K}(0)$  is initialized with an identity matrix and  $\xi_n([i, j], 0)_{K|K} = 1$  for all paths and cells (i.e., straight-ray model). At subsequent snapshots when  $t \neq 0$ , the initial state vector at iteration  $k = 0$  is set to  $\hat{\mathbf{x}}_{0|0}(t) = \hat{\mathbf{x}}_{K|K}(t-1)$ ,  $\xi_n([i, j], t)_{0|0} = \xi_n([i, j], t-1)_{K|K}$  and the corresponding covariance matrix to  $P_{0|0}(t) = P_{K|K}(t-1)$ .

2) *Generating Initial Sigma Points*: Sigma points are  $2L+1$  fixed point masses to approximate the input distribution. Using the initial estimates  $\hat{\mathbf{x}}_{k-1|k-1}(t)$  and  $P_{k-1|k-1}(t)$  for the  $k$ th iteration at time  $t$ , the sigma points are calculated as follows:

$$\begin{bmatrix} \mathbf{X}_{0,k-1|k-1}(t) \\ \vdots \\ \mathbf{X}_{i,k-1|k-1}(t) \\ \vdots \\ \mathbf{X}_{L+i,k-1|k-1}(t) \\ \vdots \end{bmatrix} = \begin{bmatrix} \hat{\mathbf{x}}_{k-1|k-1}(t) \\ \vdots \\ \hat{\mathbf{x}}_{k-1|k-1}(t) + \gamma \sqrt{P_{k-1|k-1}(t)}_{[i]} \\ \vdots \\ \hat{\mathbf{x}}_{k-1|k-1}(t) - \gamma \sqrt{P_{k-1|k-1}(t)}_{[i]} \\ \vdots \end{bmatrix}, \quad i = 1, \dots, L \quad (28)$$

where  $\gamma \approx \rho\sqrt{L}$  is a scaling parameter,  $\rho$  determines the spread of sigma points around  $\hat{\mathbf{x}}_{k-1|k-1}(t)$ , and  $\sqrt{P_{k-1|k-1}(t)}_{[i]}$  is the  $i$ th column of the Cholesky factor [36] of  $P_{k-1|k-1}(t)$ .

3) *A Priori State Estimation*: The initial sigma points are transformed through the state evolution equation (24)

$$\mathbf{X}_{i,k|k-1}^*(t) = \mathbf{A}\mathbf{X}_{i,k-1|k-1}(t) \quad i = 0, \dots, 2L. \quad (29)$$

A weighted sum of these transformed sigma points is calculated to estimate the *a priori* state estimate  $\hat{\mathbf{x}}_{k|k-1}(t)$  and the covariance matrix  $P_{k|k-1}(t)$

$$\begin{aligned} \hat{\mathbf{x}}_{k|k-1}(t) &= \sum_{i=0}^{2L} W_i^{(m)} \mathbf{X}_{i,k|k-1}^*(t) \\ P_{k|k-1}(t) &= \sum_{i=0}^{2L} W_i^{(c)} [\mathbf{X}_{i,k|k-1}^*(t) - \hat{\mathbf{x}}_{k|k-1}(t)] \\ &\quad \times [\mathbf{X}_{i,k|k-1}^*(t) - \hat{\mathbf{x}}_{k|k-1}(t)]^T + \mathbf{R}_u \end{aligned} \quad (30)$$

where the weights  $W_i^{(m)}$ s and  $W_i^{(c)}$ s are [29]  $W_0^{(m)} = \lambda/(\lambda + L)$ ,  $W_0^{(c)} = \lambda/(\lambda + L) + (1 - \rho^2 + \beta)$ , and  $W_i^{(m)} = W_i^{(c)} = 1/(2(L + \lambda))$  for  $i = 1, \dots, 2L$ , with  $\beta$  being a constant used to incorporate prior knowledge of the distribution of the state vector and is set to  $\beta = 2$  for Gaussian distribution, and  $\lambda = L(\rho^2 - 1)$  is a scaling parameter.

4) *Covariance Matrices Computation*: New sigma points are calculated based on the *a priori* state estimates  $\hat{\mathbf{x}}_{k|k-1}(t)$  and the *a priori* error covariance matrix  $P_{k|k-1}(t)$

$$\begin{bmatrix} \mathbf{X}_{0,k|k-1}(t) \\ \vdots \\ \mathbf{X}_{i,k|k-1}(t) \\ \vdots \\ \mathbf{X}_{L+i,k|k-1}(t) \\ \vdots \end{bmatrix} = \begin{bmatrix} \hat{\mathbf{x}}_{k|k-1}(t) \\ \vdots \\ \hat{\mathbf{x}}_{k|k-1}(t) + \gamma \sqrt{P_{k|k-1}(t)}_{[i]} \\ \vdots \\ \hat{\mathbf{x}}_{k|k-1}(t) - \gamma \sqrt{P_{k|k-1}(t)}_{[i]} \\ \vdots \end{bmatrix}, \quad i = 1, \dots, L. \quad (32)$$

The new sigma points are transformed through the nonlinear observation process (26) to yield

$$\Upsilon_{i,k|k-1}(t) = H(\mathbf{X}_{i,k|k-1}(t)) \quad i = 0, \dots, 2L. \quad (33)$$

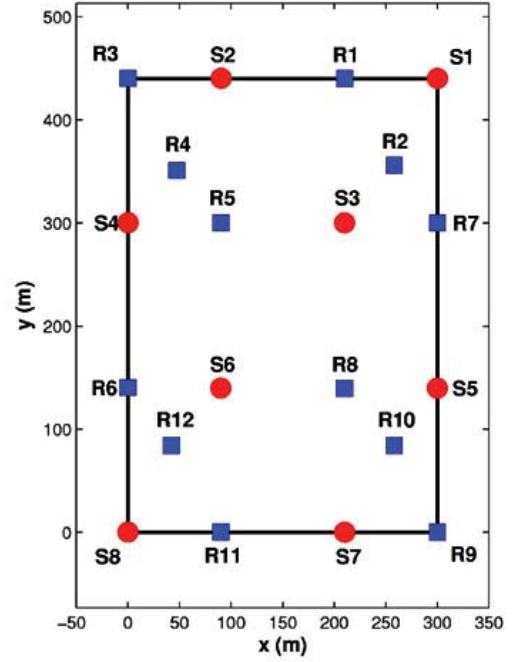


Fig. 2. Layout of the STINHO field experiment—adopted from [13].

These are then used to find  $\hat{\mathbf{y}}_{k|k-1}(t)$  and the covariance and cross-covariance matrices  $P_{yy,k}(t)$  and  $P_{xy,k}(t)$  using

$$\hat{\mathbf{y}}_{k|k-1}(t) = \sum_{i=0}^{2L} W_i^{(m)} \Upsilon_{i,k|k-1}(t) \quad (34)$$

$$P_{yy,k}(t) = \sum_{i=0}^{2L} W_i^{(c)} [\Upsilon_{i,k|k-1}(t) - \hat{\mathbf{y}}_{k|k-1}(t)] [\Upsilon_{i,k|k-1}(t) - \hat{\mathbf{y}}_{k|k-1}(t)]^T + \mathbf{R}_v \quad (35)$$

$$P_{xy,k}(t) = \sum_{i=0}^{2L} W_i^{(c)} [\mathbf{X}_{i,k|k-1}(t) - \hat{\mathbf{x}}_{k|k-1}(t)] [\Upsilon_{i,k|k-1}(t) - \hat{\mathbf{y}}_{k|k-1}(t)]^T. \quad (36)$$

5) *Kalman Gain Computation and a Posteriori State Estimation*: These are used to generate the Kalman gain  $\mathbf{K}_k(t)$ , a *posteriori* state vector  $\hat{\mathbf{x}}_{k|k}(t)$   $\zeta_n([i, j], t)_{k|k}$ , and the *a posteriori* error covariance matrix  $P_{k|k}(t)$  estimates as follows:

$$\mathbf{K}_k(t) = P_{xy,k}(t)P_{yy,k}^{-1}(t) \quad (37)$$

$$\hat{\mathbf{x}}_{k|k}(t) = \hat{\mathbf{x}}_{k|k-1}(t) + \mathbf{K}_k(t)[\mathbf{y}_t - \hat{\mathbf{y}}_{k|k-1}(t)] \quad (38)$$

$$P_{k|k}(t) = P_{k|k-1}(t) - \mathbf{K}_k(t)P_{yy,k}(t)\mathbf{K}_k^T(t) \quad (39)$$

$$\mathbf{s}_n([i, j], t)_{k|k} = \frac{\mathbf{n}_n([i, j], t)\hat{c}_L([i, j], t)_{k|k} + \hat{\mathbf{v}}([i, j], t)_{k|k}}{\|\mathbf{n}_n([i, j], t)\hat{c}_L([i, j], t)_{k|k} + \hat{\mathbf{v}}([i, j], t)_{k|k}\|} \quad (40)$$

where  $\hat{c}_L([i, j], t)_{k|k}$ s and  $\hat{\mathbf{v}}([i, j], t)_{k|k}$ s are extracted from the state estimate  $\hat{\mathbf{x}}_{k|k}(t)$  and  $\zeta_n([i, j], t)_{k|k} = \mathbf{s}_n([i, j], t)_{k|k} \cdot \mathbf{n}_n([i, j], t)$ . Note that here  $\mathbf{s}_n([i, j], t)$  is updated during the fixed iteration process as well as over time. This allows for a more accurate ray-tracing procedure.

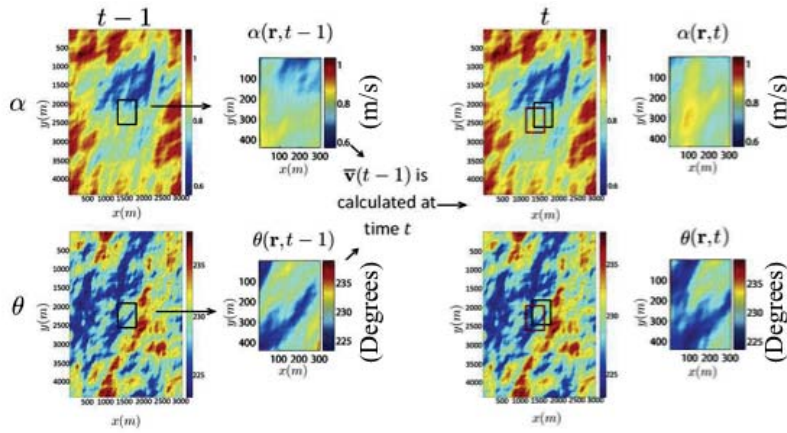


Fig. 3. Oversized  $\alpha$  and  $\theta$  fields and the process of generating the data sequence in time.

6) *Iteration Step*: If  $k < K$ , then the algorithm proceeds to the next iteration  $k + 1$  on the fixed snapshot  $t$  and redo steps 2 to 5. But if  $k = K$ , then it proceeds in time  $t + 1$  and jumps to step 1.

#### IV. NUMERICAL RESULTS AND BENCHMARKING

In order to test our proposed UKF-based algorithm, a dataset was acquired from the University of Leipzig, collected at the Meteorological Observatory, Lindenberg, Germany, as part of the STINHO project. The detailed explanation of this experiment can be found in [37]. Fig. 2 shows the layout of the investigation area used in the STINHO project and the locations of the receivers and transmitters, indicated by  $R_i$  and  $S_i$ , respectively. The investigation area is of size  $300 \text{ m} \times 440 \text{ m}$  and there were 8 transmitters and 12 receivers, as can be seen in Fig. 2. In the absence of sufficient *in situ* measurements to conduct a comprehensive evaluation and benchmarking of the developed algorithm with the TDSI method, a synthetic dataset with similar characteristics (e.g., range of values) is generated and used in this paper. Clearly, there exist many different models to generate synthetic wind velocity and temperature fields, e.g., the commonly used Navier–Stokes equation of motion [38], [39]. However, in this paper a simple yet realistic statistical model is employed to generate these fields using the 2-D extension of fBm model [30]. This procedure is described next.

##### A. Synthetic Data Generation

There are several mathematical models that can be used to describe the wind power spectrum [40]–[46]. One such model is the fBm [46], which is also known as  $1/f$  noise [47]. In this paper, we have used an fBm-based method inspired by [30] to generate 2-D wind velocity and temperature fields. The power spectral density (PSD) of a 1-D fBm is defined as

$$S(f) = \frac{1}{f^\beta} \quad (41)$$

where  $f$  is frequency (in Hz) and  $0 < \beta < 2$  is known as noise roughness which is usually chosen close to 1. Note

that  $\beta = 0$  and  $\beta = 2$  represent white noise and Brownian motion (random walk) noise, respectively. Based on the fBm, the method in [30] suggests a 2-D PSD function as

$$S(f_1, f_2) = \frac{\vartheta}{(f_1^2 + f_2^2)^{\beta+1}} \quad (42)$$

where  $f_1$  and  $f_2$  are the 2-D spatial frequencies ( $m^{-1}$ ),  $\beta = 1.66$  for wind field simulations (though it can be changed to obtain wind and temperature fields with different characteristics), and  $\vartheta$  is a constant which depends on the height of the simulated field from the ground and the type of the terrain.

The fields  $\mathbf{c}_L(\mathbf{r}, t_0)$ ,  $\alpha(\mathbf{r}, t_0)$ , and  $\theta(\mathbf{r}, t_0)$  are then generated using (42) based on the algorithm developed in [48] for an area 10 times bigger than the investigation area, i.e.,  $3000 \text{ m} \times 4400 \text{ m}$  with 1-m spatial resolution at initial time  $t_0$ . The investigation area (same size as that in the STINHO experiment [37]) is located at the center of this larger field. Given these fields at initial time  $t_0$ , the wind velocity and temperature fields are calculated in the investigation area at time  $t$  assuming the frozen turbulence using

$$\mathbf{v}(\mathbf{r}, t) = \mathbf{v}(\mathbf{r} - \bar{\mathbf{v}}(t-1)\Delta t, t-1) \quad (43)$$

$$\mathbf{c}_L(\mathbf{r}, t) = \mathbf{c}_L(\mathbf{r} - \bar{\mathbf{v}}(t-1)\Delta t, t-1) \quad (44)$$

where  $\bar{\mathbf{v}}(t)$  is the spatial mean wind velocity vector at time  $t$ . Fig. 3 shows the larger size field and the process of generating the synthetic data in time. Note that the frozen turbulence hypothesis includes two assumptions about the temporal evolution of the atmosphere. First, the layers of the fields are spatially stable through time; and second, these layers are moving with the spatial mean wind velocity.

The synthetic data is generated for 500 consecutive snapshots of wind velocity and temperature fields with the same spatial resolution of 1 m and temporal resolution of  $\Delta t = 12 \text{ s}$ . The travel time for each sound ray path is then calculated using (26) at each snapshot with the same resolution of 1 m. Fig. 4 shows the synthetically generated wind velocity and temperature fields for a sample snapshot ( $t = 75$ ) over the investigation area. The reconstruction results of the developed method and TDSI are presented next.

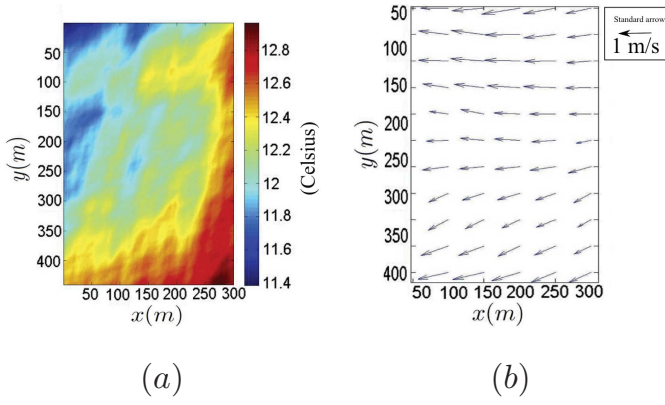


Fig. 4. (a) Synthetic temperature field. (b) Synthetic wind velocity field.

### B. Reconstruction Results on Synthetic Dataset

In this section, TDSI and UKF-based acoustic tomography algorithms are applied to reconstruct temperature and wind velocity fields in the synthesized data described above. The investigation area was divided into  $4 \times 8$  reconstruction grids each of size  $75 \text{ m} \times 55 \text{ m}$ . Note that the reconstruction resolution is such that the total number of states ( $32 \times 3$ ) in the UKF is the same number of propagation paths as in the STINHO experiment (i.e., a total of 96 paths) and hence is substantially worse than the spatial resolution used to generate the synthetic data. Clearly, increasing the reconstruction resolution (or decreasing the grid size) would have caused some state variables to become decoupled from the observation equation (i.e., unobservable). The travel times are corrupted using an additive measurement noise vector  $\mathbf{v}_t$  which is assumed to be a zero-mean white Gaussian process with covariance matrix  $\mathbf{R}_v = \sigma_v^2 \mathbf{I}$  and  $\sigma_v^2 = 0.01$ . This variance is chosen on the basis of the uncertainty measurements reported in [37], which is 0.3 ms for each travel time measurement on a single ray path measurement. The noisy travel times of all the paths are used as the observation vector at every snapshot. The reconstruction results are then compared in terms of reconstruction accuracy, tracking ability, and speed. Note that, because of the lack of direction of arrival measurements in the STINHO experiment and low wind conditions, we also assumed straight-ray models.

The mean fields at each snapshot are first calculated using the method described in Section II-B. Fig. 5 shows the plots of the actual and calculated mean fields at all snapshots for the temperature, wind velocity amplitude, and wind velocity angle. The red curve is the actual mean field calculated from the synthetic data over 500 snapshots, and the green curve is the reconstructed mean field. These results illustrate the accuracy of mean field estimation process in [6] and [13].

1) *TDSI-Based Acoustic Tomography*: The first five snapshots of the synthesized data were used as the training data to estimate the parameters of the adiabatic sound speed, wind velocity amplitude, and wind velocity angle spatial covariance functions. The Gaussian spatial covariance function is considered here. That is, for the adiabatic sound speed, the spatial covariance function is

$$B_{c_{LC_L}^s}(\mathbf{r}_l, \mathbf{r}_k) = \sigma_{c_L}^2 \exp\left(-\frac{(\mathbf{r}_l - \mathbf{r}_k)^2}{l_{c_L}^2}\right) \quad (45)$$

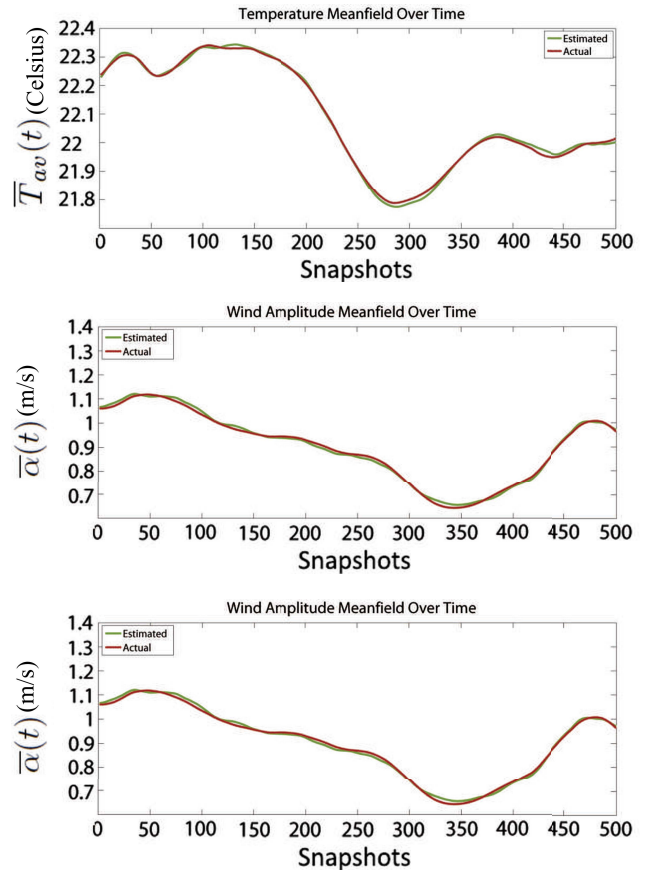


Fig. 5. Actual and estimated mean temperature, wind velocity amplitude, and wind velocity angle fields over all 500 snapshots.

where  $\mathbf{r}_l$  and  $\mathbf{r}_k$  are location vectors,  $\sigma_{c_L}^2$  is the variance, and  $l_{c_L}$  is the correlation length. Maximum likelihood (ML) method [24] was used to estimate these parameters from the training data corresponding to the  $4 \times 8$  grid located approximately in the middle of the investigation area. Note that the high-resolution data was not used here because in realistic situations this high-resolution data is not available for measurement. Similar spatial covariance functions can be defined for the wind velocity fields according to [13, eqs. (31)–(34)].

The spatiotemporal covariance functions are constructed on the basis of the frozen turbulence assumption and the estimated spatial covariance functions. For instance, spatiotemporal covariance of the adiabatic sound speed is defined as

$$B_{c_{LC_L}^s}(\mathbf{r}_l, t_l, \mathbf{r}_k, t_k) = B_{c_{LC_L}^s}(\mathbf{r}_l, \mathbf{r}_k - \bar{\mathbf{v}}(t_l)(t_k - t_l)) \quad (46)$$

where  $B_{c_{LC_L}^s}(\mathbf{r}_l, t_l, \mathbf{r}_k, t_k)$  is the spatiotemporal covariance of the adiabatic sound speed field at locations  $\mathbf{r}_l$  and  $\mathbf{r}_k$  and at times  $t_l$  and  $t_k$ , and  $\bar{\mathbf{v}}(t_l)$  is the spatial mean wind velocity vector at time  $t_l$ . The spatiotemporal covariances of wind velocity amplitude  $B_{\alpha\alpha}$  and wind velocity angle  $B_{\theta\theta}$  are obtained similarly.

Having estimated the spatiotemporal covariance matrices,  $C_{mq_a}$  and  $C_{qa_qa}$  matrices are then generated at each snapshot according to [13, eqs. (18)–(21)]. Several values for number of previous snapshots,  $M$ , was tried, and  $M = 4$  was found to be the optimal choice as far as the reconstruction accuracy and processing speed are concerned. Thus,  $M = 4$  was

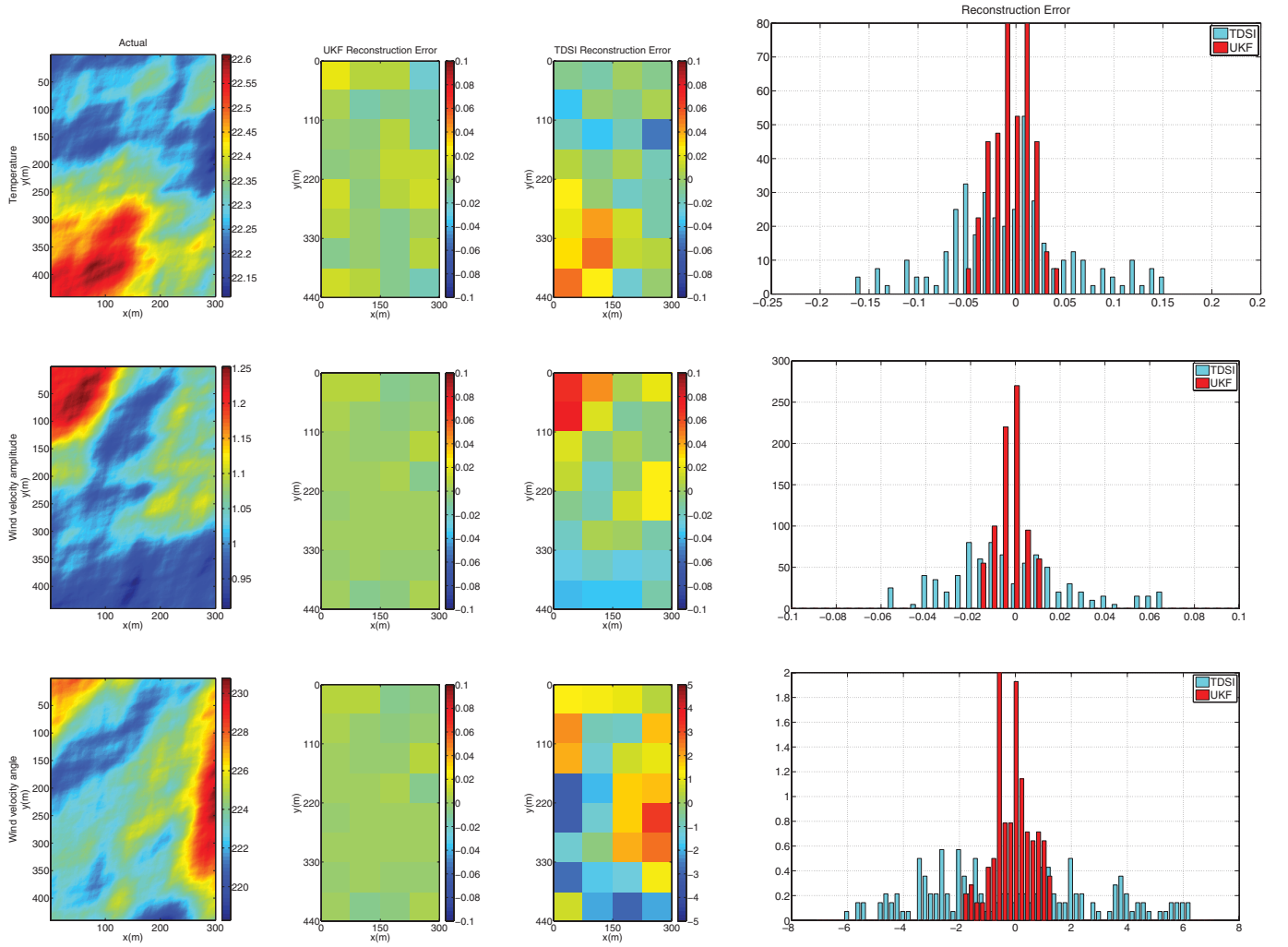


Fig. 6. Comparison of field reconstructions using TDSI and UKF-based acoustic tomography methods for snapshot number 100. The histogram is plotted for reconstruction errors of snapshots 98 through 102.

used to generate the augmented observation vector  $\mathbf{q}_a(t) = [\mathbf{q}^T(t-4), \mathbf{q}^T(t-3), \mathbf{q}^T(t-2), \mathbf{q}^T(t-1), \mathbf{q}^T(t)]^T$  and to reconstruct the fluctuation fields at time  $t$ . The fluctuation fields are generated using (13) and subsequently added to the mean fields to produce the final reconstructed fields at snapshot  $t$ .

2) *UKF-Based Acoustic Tomography*: The same Gaussian spatial covariance functions with the ML-estimated parameters for the TDSI method were also used to estimate the 3-D AR model coefficients and covariance matrix  $R_u$ . Using the Yule-Walker method [34], the 3-D AR coefficients are estimated to be  $\rho_0^{(cL)} = 0.8482$ ,  $\rho_1^{(cL)} = 0.0777$ ,  $\rho_2^{(cL)} = -0.0397$ ,  $\rho_0^{(\alpha)} = 0.9983$ ,  $\rho_1^{(\alpha)} = -0.0086$ , and  $\rho_2^{(\alpha)} = 0.0091$  for the adiabatic sound speed and wind velocity amplitude models, respectively. Random walk model is used for wind velocity angle (i.e.,  $\rho_0^{(\theta)} = 1$ ,  $\rho_1^{(\theta)} = 0$  and  $\rho_2^{(\theta)} = 0$ ) as mentioned before.

The mean fields calculated at time  $t_0$  are used as the initial state,  $\mathbf{x}_{0|0} = [\bar{c}_L^T(t_0), \bar{\alpha}^T(t_0), \bar{\theta}^T(t_0)]^T$ , and further  $P_{0|0} = \mathbf{I}$ . Then, the temperature, wind velocity amplitude, and angle fields are reconstructed using steps 1–5 of the iterated UKF for  $K = 3$  number of fixed-point iterations.

Figs. 6–8 illustrate the actual and field reconstruction errors using TDSI and UKF-based acoustic tomography methods for three selected snapshots  $t = 100, 175$ , and  $250$  of the synthetic dataset, respectively. The errors are calculated by comparing the reconstructed field for each state (at a grid) with the spatially averaged value of the fields over the corresponding  $75 \text{ m} \times 55 \text{ m}$  area. The histograms of these reconstruction errors are also plotted to demonstrate the distribution of the reconstruction errors for both methods. It can be seen that both methods reconstruct the fields fairly well. However, the UKF-based method produces somewhat more accurate results, especially for the temperature field. Additionally, the computational complexity of UKF-based acoustic tomography method is significantly lower than that of the TDSI method. The computational complexity of the UKF-based acoustic tomography method is  $O(L^3)$  with  $L = 3 * I * J = 96$ , being the dimension of the state space. For TDSI, on the other hand, this computational complexity is  $O([(M+1) * N]^3)$ , where  $(M+1)N = 480$  is the size of the augmented observation vector. The computation time for the iterated UKF for  $K = 3$  at every snapshot was found to be approximately 5 s on a computer with an Intel Core i7 CPU, 12.0 GB RAM, and 64-b

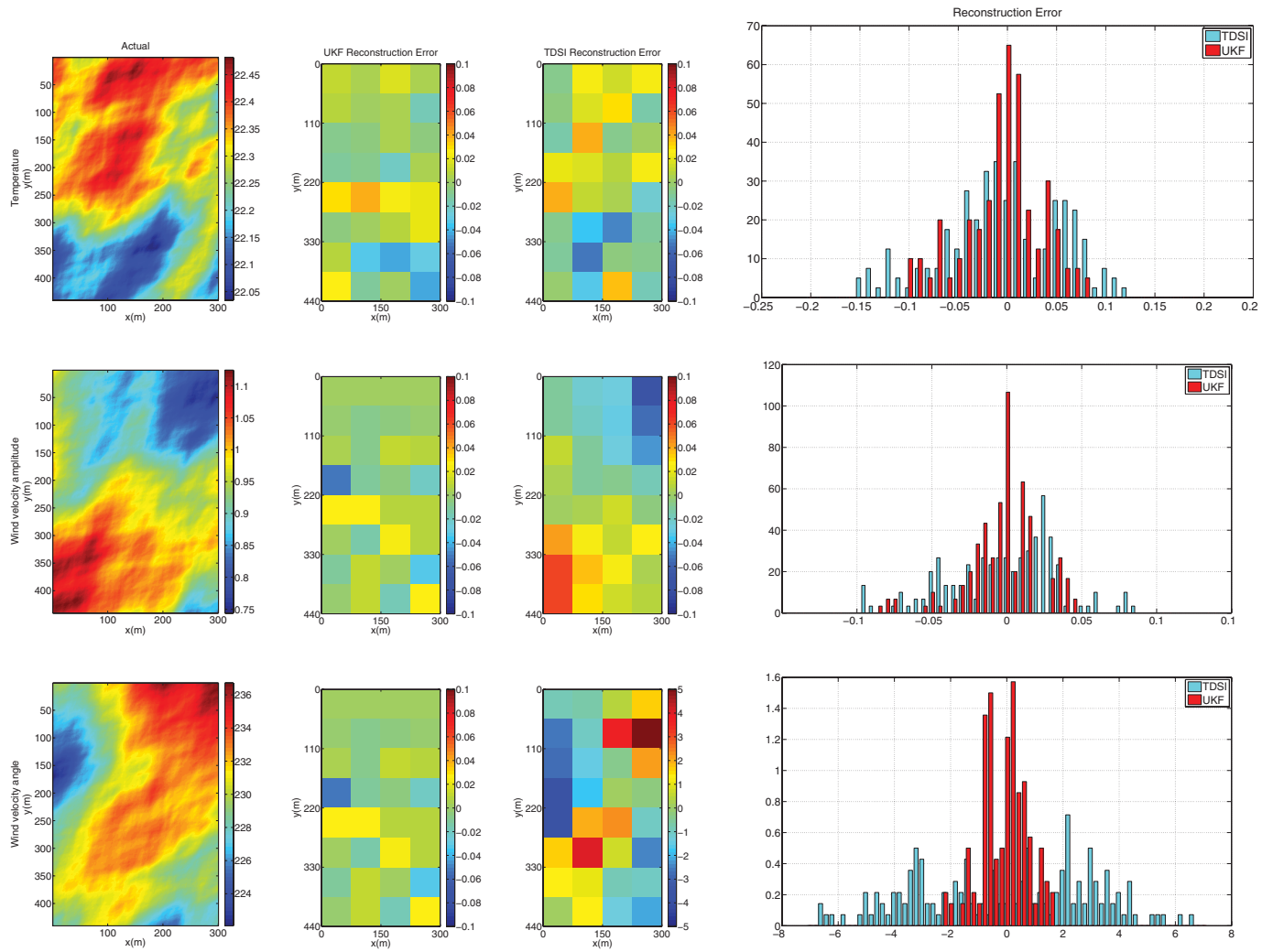


Fig. 7. Comparison of field reconstructions using TDSI and UKF-based acoustic tomography methods for snapshot number 175. The histogram is plotted for reconstruction errors of snapshots 173 through 177.

operating system, while it takes approximately 200 s for the TDSI method.

In order to compare the performance of TDSI and UKF-based acoustic tomography over time, the reconstruction errors for each field at every snapshot are computed and used in the box plots shown in Fig. 9 for temperature, wind velocity amplitude, and wind velocity angle fields. Each box demonstrates the reconstruction errors at a single snapshot, while the central mark is the median, the edges of the box plot are 25th and 75th percentiles and the whiskers extend to the most extreme points, while outliers are plotted individually as small circles. From this figure, it can clearly be seen that the UKF-based acoustic tomography method reconstructs the fields more accurately, especially when there is drastic change in the fields. Snapshots 120–200 (24–40 min) in wind velocity amplitude reconstruction and 310–400 (62–80 min) in wind velocity angle reconstruction are the time periods in which the synthetic wind velocity field exhibited drastic change in both amplitude and angle. It can be seen that the UKF-based method is better able to track these changes that occur in a short period of time.

## V. CONCLUSION

In this paper, a new statistical-based approach was proposed for the acoustic tomography of the atmosphere. The problem was formulated as a nonlinear state estimation where state variables were temperature and wind velocity amplitude and angle in each grid. Assuming that angles of departure/arrival can be measured using tripoles of transmitters and receivers at each sensor site, an iterative ray tracing procedure was also adopted and incorporated with the state estimation problem. The problem formulation was then presented, and UKF was employed to estimate the states at every snapshot given the measured travel times.

To evaluate the performance of the developed algorithm, a synthetic dataset of temperature and wind velocity fields was generated on the basis of the fBm method for 500 snapshots, with spatial resolution of 1 m and temporal resolution of 12 s assuming low wind conditions. The proposed method was benchmarked on this dataset against the TDSI method, and the reconstruction errors for temperature and wind velocity fields for each method were presented. The performance of the two methods was then compared using the statistics

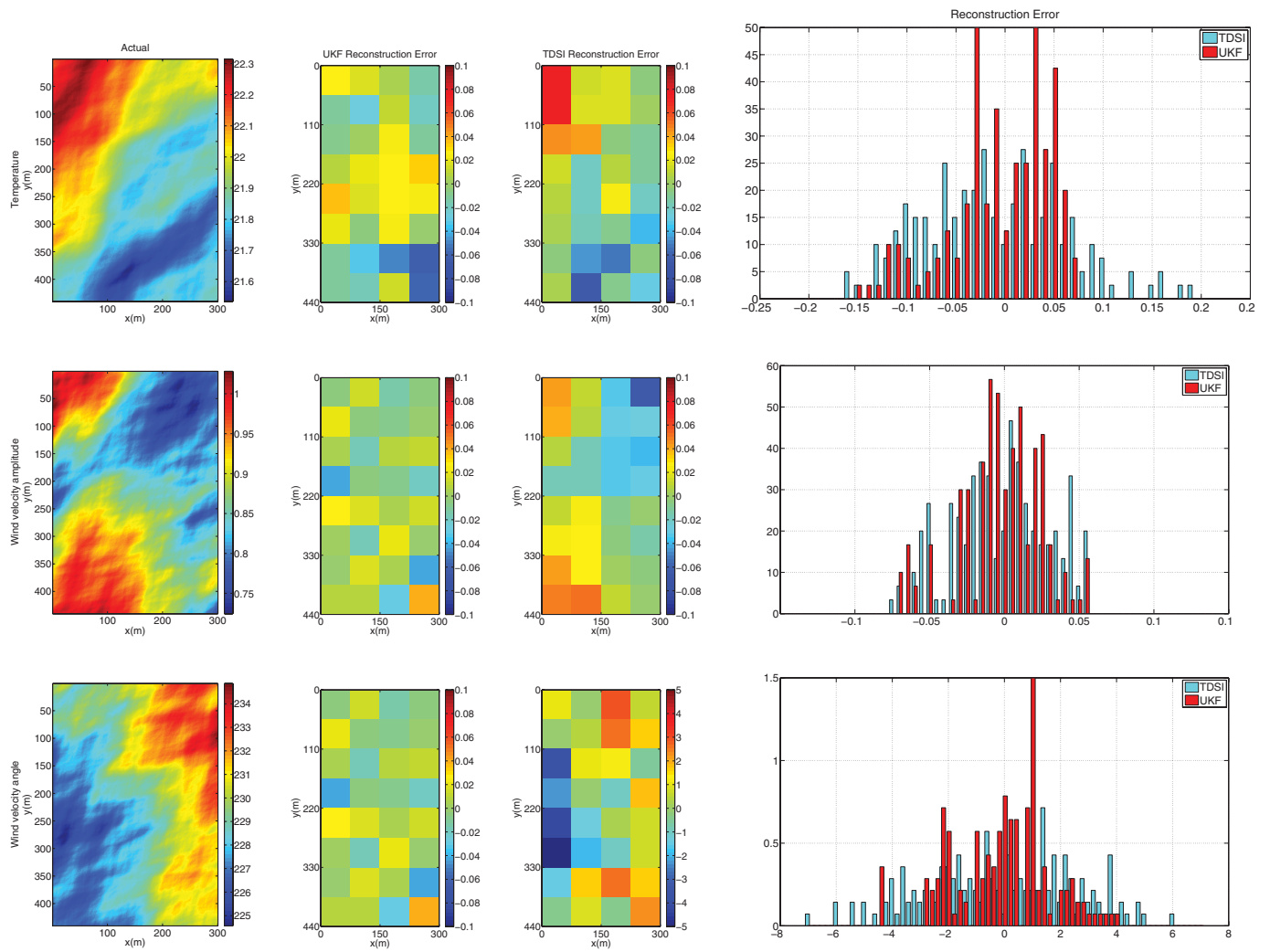


Fig. 8. Comparison of field reconstructions using TDSI and UKF-based acoustic tomography methods for snapshot number 250. The histogram is plotted for reconstruction errors of snapshots 248 through 252.

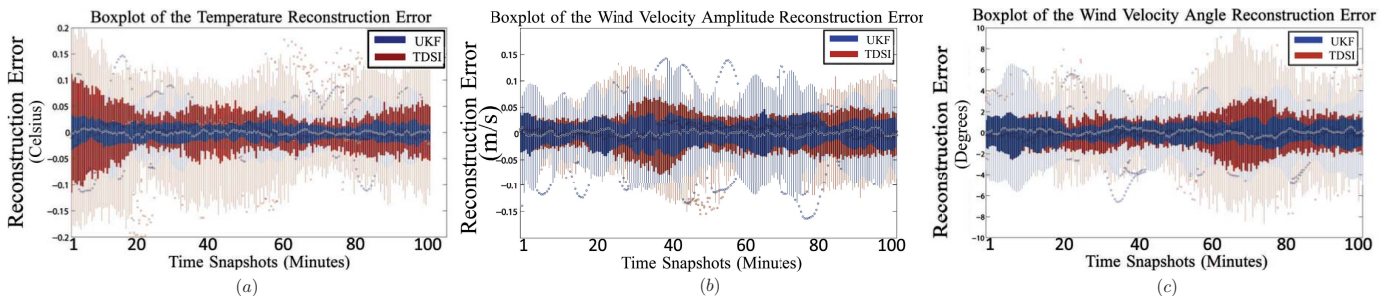


Fig. 9. Comparison of field reconstruction errors of TDSI and UKF-based acoustic tomography methods in (a) temperature, (b) wind velocity amplitude, and (c) wind velocity angle reconstruction over all snapshots.

of the reconstruction error for each field. It was shown that UKF-based acoustic tomography method offers certain benefits over the TDSI method. The reconstructed fields using UKF-based tomography were found to be more accurate than those generated using the TDSI method. This was especially true for the temperature field. Additionally, due to the nature of the UKF, the proposed method can be applied to applications where near-real-time monitoring of the investigation area is needed. Application and evaluation of the proposed method to nonlinear atmospheric tomography problems is an area for future research.

ACKNOWLEDGMENT

The authors would like to thank A. Raabe and K. Arnold at the Leipzig Institute for Meteorology, University of Leipzig, Leipzig, Germany, for acoustic measurements.

REFERENCES

- [1] S. Bradley, *Atmospheric Acoustic Remote Sensing*. Boca Raton, FL, USA: CRC Press, 2008.
- [2] V. E. Ostashev, S. N. Vecherin, D. K. Wilson, A. Ziemann, and G. H. Goedecke, "Recent progress in acoustic travel-time tomography of the atmospheric surface layer," *Meteorologische Zeitschrift*, vol. 18, no. 2, pp. 125–133, Apr. 2009.

- [3] S. Weinbrecht, S. Raasch, A. Ziemann, K. Arnold, and A. Raabe, "Comparison of large-eddy simulation data with spatially averaged measurements obtained by acoustic tomography—Presuppositions and first results," *Boundary Layer Meteorol.*, vol. 111, no. 3, pp. 441–465, Jun. 2004.
- [4] V. Ostashev, *Acoustics in Moving Inhomogeneous Media*. London, U.K.: E & FN Spon, 1997.
- [5] P. Blanc-Benon, B. Lipkens, L. Dallois, M. F. Hamilton, and D. T. Blackstock, "Propagation of finite amplitude sound through turbulence: Modeling with geometrical acoustics and the parabolic approximation," *J. Acoust. Soc. Amer.*, vol. 111, no. 1, pp. 487–498, 2002.
- [6] D. K. Wilson and D. W. Thomson, "Acoustic tomographic monitoring of the atmospheric surface layer," *Atmosph. Ocean. Technol.*, vol. 11, no. 3, pp. 751–769, Jun. 1994.
- [7] S. Vogt and P. Thomas, "SODAR—A useful remote sounder to measure wind and turbulence," *J. Wind Eng. Ind. Aerodynamics*, vols. 54–55, pp. 163–172, Feb. 1995.
- [8] E. R. Westwater, Y. Han, V. G. Irisov, V. Leuskiy, E. N. Kadygrov, and S. A. Viazankin, "Remote sensing of boundary layer temperature profiles by a scanning 5-mm microwave radiometer and RASS: A comparison experiments," *J. Atmosph. Ocean. Technol.*, vol. 16, no. 7, pp. 805–818, Jul. 1999.
- [9] G. J. Kunz, "Vertical atmospheric profiles measured with LIDAR," *Appl. Opt.*, vol. 22, no. 13, pp. 1955–1957, Jun. 1983.
- [10] D. K. Wilson, A. Ziemann, V. E. Ostashev, and A. G. Voronovich, "An overview of acoustic travel-time tomography in the atmosphere and its potential applications," *Acustica*, vol. 87, no. 6, pp. 721–730, 2001.
- [11] A. Ziemann, K. Arnold, and A. Raabe, "Acoustic travel time tomography—A method for remote sensing of the atmospheric surface layer," *Meteorol. Atmosph. Phys.*, vol. 71, pp. 43–51, Apr. 1999.
- [12] K. Arnold, A. Ziemann, A. Raabe, and G. Spindler, "Acoustic tomography and conventional meteorological measurements over heterogeneous surfaces," *Meteorol. Atmosph. Phys.*, vol. 85, nos. 1–3, pp. 175–186, Jan. 2004.
- [13] S. N. Vecherin, V. E. Ostashev, G. H. Goedecke, D. K. Wilson, and A. G. Voronovich, "Time-dependent stochastic inversion in acoustic travel-time tomography of the atmosphere," *J. Acoust. Soc. Amer.*, vol. 119, no. 5, pp. 2579–2588, May 2006.
- [14] S. N. Vecherin, V. E. Ostashev, A. Ziemann, D. K. Wilson, K. Arnold, and M. Barth, "Tomographic reconstruction of atmospheric turbulence with the use of time-dependent stochastic inversion," *J. Acoust. Soc. Amer.*, vol. 122, no. 3, pp. 1416–1425, 2007.
- [15] M. McCarron, M. R. Azimi-Sadjadi, and M. Mungiole, "An operationally adaptive system for rapid acoustic transmission loss prediction," *Neural Netw.*, vol. 27, pp. 91–99, Mar. 2012.
- [16] W. Munk, P. Worcester, and C. Wunsch, *Ocean Acoustic Tomography*. Cambridge, U.K.: Cambridge Univ. Press, 1995.
- [17] W. Munk and C. Wunsch, "Ocean acoustic tomography: A scheme for large-scale monitoring," *Deep Sea Res.*, vol. 26, no. 2, pp. 123–161, 1979.
- [18] J. L. Spiesberger and K. M. Fristrup, "Passive localization of calling animals and sensing of their acoustic environment using acoustic tomography," *Amer. Naturalist*, vol. 135, no. 1, pp. 107–153, Jan. 1990.
- [19] E. Piccolomini, "The conjugate gradient regularization method in computed tomography problems," *Appl. Math. Comput.*, vol. 102, no. 1, pp. 87–99, Jan. 1999.
- [20] K. Arnold, A. Ziemann, and A. Raabe, "Tomographic monitoring of wind and temperature at different heights above the ground," *Acustica*, vol. 87, no. 6, pp. 703–708, Nov.–Dec. 2001.
- [21] I. Jovanovic, A. Hormati, L. Sbaiz, and M. Vetterli, "Efficient and stable acoustic tomography using sparse reconstruction methods," in *Proc. 19th Int. Congr.*, Sep. 2007, pp. 2–7.
- [22] A. H. Andersen and A. C. Kak, "Simultaneous algebraic reconstruction technique (SART): A superior implementation of the ART algorithm," *Ultrason. Imaging*, vol. 6, no. 1, pp. 81–94, Jan. 1984.
- [23] I. Jovanovic, "Acoustic tomography for scalar and vector fields: Theory and application to temperature and wind estimation," *J. Atmosph. Ocean. Technol.*, vol. 26, no. 8, pp. 1–15, Aug. 2009.
- [24] L. Scharf, *Statistical Signal Processing: Detection, Estimation, and Time Series Analysis*. Reading, MA, USA: Addison-Wesley, 1991.
- [25] S. Kodali, K. Deb, P. Munshi, and N. Kishore, "Comparing GA with MART to tomographic reconstruction of ultrasound images with and without noisy input data," in *Proc. IEEE Congr. Evol. Comput.*, May 2009, pp. 2963–2970.
- [26] M. Barth and A. Raabe, "Acoustic tomographic imaging of temperature and flow fields in air," *Meas. Sci. Technol.*, vol. 22, no. 3, pp. 2579–2588, Mar. 2011.
- [27] C. Yardim, P. Gerstoft, and W. S. Hodgkiss, "Tracking of geoaoustic parameters using kalman and particle filters," *J. Acoust. Soc. Amer.*, vol. 125, no. 2, pp. 746–760, Feb. 2009.
- [28] S. Julier and J. Uhlmann, "Unscented filtering and nonlinear estimation," *Proc. IEEE*, vol. 92, no. 3, pp. 401–422, Mar. 2004.
- [29] E. A. Wan and R. V. Merwe, "The unscented Kalman filter," in *Kalman Filtering and Neural Networks*, S. S. Haykin, Ed. New York, NY, USA: Wiley, 2001, ch. 7, pp. 221–277.
- [30] O. Khorloo, Z. Gunjee, and B. Sosorbaram, "Wind field synthesis for animating wind-induced vibration," *Int. J. Virtual Reality*, vol. 10, no. 1, pp. 53–60, Feb. 2011.
- [31] R. E. Kalman, "A new approach to linear filtering and prediction problems," *J. Basic Eng.*, vol. 82, no. 1, p. 35–45, 1960.
- [32] G. Welch and G. Bishop, "An introduction to the Kalman filter," *Design*, vol. 7, pp. 1–16, Feb. 2001.
- [33] S. Julier and J. K. Uhlmann, "A general method for approximating nonlinear transformations of probability distributions," *Transformation*, vol. 4, pp. 1–27, Jan. 1996.
- [34] P. J. Brockwell and R. A. Davis, *Introduction to Time Series and Forecasting*, vol. 39. New York, NY, USA: Springer-Verlag, 2002.
- [35] R. Zhan and J. Wan, "Iterated unscented Kalman filter for passive target tracking," *IEEE Trans. Aerosp. Electron. Syst.*, vol. 43, no. 3, pp. 1155–1163, Jul. 2007.
- [36] R. B. Schnabel and E. Eskow, "A new modified Cholesky factorization," *SIAM J. Sci. Comput.*, vol. 11, no. 6, pp. 1136–1158, 1990.
- [37] A. Raabe, A. Klaus, A. Ziemann, M. Schroeter, S. Raasch, J. Bange, P. Zittel, T. Spiess, T. Foken, M. Goeckede, F. Beyrich, and J. P. Lepp, "STINHO—Structure of turbulent transport under inhomogeneous surface conditions," *Meteorologische Zeitschrift*, vol. 14, no. 3, pp. 315–327, Jun. 2005.
- [38] J. Mann, "Wind field simulation," *Probabilistic Eng. Mech.*, vol. 13, no. 4, pp. 269–282, Oct. 1998.
- [39] H. G. Kim, V. C. Patel, and C. M. Lee, "Numerical simulation of wind flow over hilly terrain," *J. Wind Eng. Ind. Aerodynamics*, vol. 87, no. 1, pp. 45–60, Sep. 2000.
- [40] M. Shinya and A. Fournier, "Stochastic motion—Motion under the influence of wind," *Computer Graphics Forum*, vol. 11, 1992.
- [41] J. Stam and F. Eugene, "Turbulent wind fields for gaseous phenomena," in *Proc. 20th Annu. Conf. Comput. Graph. Interact. Tech.*, 1993, pp. 369–376.
- [42] J. Stam, "Stable fluids," in *Proc. 26th Annu. Conf. Comput. Graph. Interact. Tech.*, 1999, pp. 121–128.
- [43] N. Foster and D. Metaxas, "Modeling the motion of a hot, turbulent gas," in *Proc. 24th Annu. Conf. Comput. Graph. Interact. Tech.*, 1997, pp. 181–188.
- [44] J. C. Kaimal and J. J. Finnigan, *Atmospheric Boundary Layer Flows: Their Structure and Measurement*, vol. 72. London, U.K.: Oxford Univ. Press, 1994.
- [45] G. H. Goedecke, V. E. Ostashev, D. K. Wilson, and H. J. Auvermann, "Quasi-wavelet model of von-Kármán spectrum of turbulent velocity fluctuations," *Boundary Layer Meteorol.*, vol. 112, no. 1, pp. 33–56, 2003.
- [46] A. N. Kolmogorov, "The local structure of turbulence in incompressible viscous fluid for very large Reynolds numbers," *Doklady Akademiia Nauk SSSR*, vol. 30, no. 4, pp. 301–305, 1941.
- [47] M. Keshner, "1/f noise," *Proc. IEEE*, vol. 70, no. 3, pp. 212–218, Mar. 1982.
- [48] H.-O. Peitgen, D. Saupe, Y. Fisher, M. McGuire, R. F. Voss, M. F. Barnsley, R. L. Devaney, and B. B. Mandelbrot, *The Science of Fractal Images*, vol. 65. New York, NY, USA: Springer-Verlag, 1988.
- [49] H. L. Van Trees, *Optimum Array Processing*, vol. 4. New York, NY, USA: Wiley, 2002.



**Soheil Kolouri** received the M.Sc. degree in electrical engineering from Colorado State University (CSU), Fort Collins, CO, USA, in 2012, with specialization in signal/image processing.

He was a Research Assistant with the Signal/Image Processing Laboratory, CSU, from 2010 to 2012. He is currently pursuing the Ph.D. degree with the Biomedical Engineering Department, Carnegie Mellon University, Pittsburgh, PA, USA.



**Mahmood Reza Azimi-Sadjadi** (SM'–89) received the M.S. and Ph.D. degrees from the Imperial College of Science and Technology, University of London, London, U.K., in 1978 and 1982, respectively, both in electrical engineering with specialization in digital signal/image processing.

He is currently a Full Professor with the Electrical and Computer Engineering Department, Colorado State University (CSU), Fort Collins, CO, USA. He is also serving as the Director of the Digital Signal/Image Laboratory, CSU. He has co-authored

the book *Digital Filtering in One and Two Dimensions* (Plenum Press, 1989). His current research interests include statistical signal and image processing, target detection, classification and tracking, sensor array processing, machine learning, and distributed sensor networks.

Dr. Azimi-Sadjadi served as an Associate Editor of the IEEE TRANSACTIONS ON SIGNAL PROCESSING and the IEEE TRANSACTIONS ON NEURAL NETWORKS.



**Astrid Ziemann** received the Diploma degree in meteorology from the Humboldt-University Berlin, Berlin, Germany, in 1996, and the Ph.D. degree (Dr. rer. nat.) from the University Leipzig, Leipzig, Germany, in 2000.

She was a Research Associate with the University Leipzig, Institute for Meteorology, from 1996 to 2004, before she assumed the position of a Junior Professor (Assistant Professor) of meteorology-remote sensing with the University of Leipzig until 2010. From 2010 to 2011, she was a Research Associate

with the Leibniz-Institute for Tropospheric Research and Guest Scientist with the Helmholtz-Centre for Environmental Research, Leipzig, before she moved to the Technical University, Dresden, Germany, Chair of Meteorology, where she works as a Scientist and Project Leader. Her current research interests include acoustic remote sensing, especially acoustic tomography at various scales, atmospheric acoustics, and atmospheric boundary layer studies in urban, rural, and forest areas.

Dr. Ziemann is a longtime member of the German Meteorological Society, where she has held several offices. She is a member of the German standardization Committee to the outdoor sound propagation and acts as an expert Auditor of the national accreditation body for the Federal Republic of Germany.